From "Digital Mapping Techniques '10—Workshop Proceedings"
U.S. Geological Survey Open-File Report 2012–1171
http://pubs.usgs.gov/of/2012/1171/

Utility of Combined Aerial Photography and Digital Imagery for Fault Trace Mapping in Diverse Terrain and Vegetation Regimes

By Jerome A. Treiman[1], Florante G. Perez[2], and William A. Bryant[3]

[1]California Geological Survey
888 S. Figueroa Street, Suite 475
Los Angeles, CA 90017
Telephone: (213) 239-0889
Fax: (213) 239-0894
email: *jtreiman@consrv.ca.gov*

[2]California Geological Survey
801 K Street, MS 12-32
Sacramento, CA 95814
Telephone: (916) 322-0203
Fax: (916) 322-4765
email: *aperez@consrv.ca.gov*

[3]California Geological Survey
801 K Street, MS 12-32
Sacramento, CA 95814
Telephone: (916) 323-9672
Fax: (916) 445-3334
email: *wbryant@consrv.ca.gov*

Introduction

Various types of aerial imagery have long been recognized for their value in fault trace mapping. Most recently, the value of LiDAR imagery to "see through" vegetation has been recognized for forested areas. In this study we compared the effectiveness of shaded relief imagery derived from high-resolution LiDAR digital elevation models to standard aerial photography and to digital multi-spectral imagery for identifying and mapping active faults in moderate to sparsely vegetated terrain in southern California. The digital imagery included recently acquired stereo imagery. We also compared LiDAR-derived imagery to several combinations of draped or fused digital imagery. Additionally, we looked at the use of accurately georeferenced digital imagery for the registration of interpreted data from older, non-registered aerial photography. The study areas spanned varying terrain and geology.

A detailed discussion of the original mapping, imagery preparation and processing, image visualization and analysis, and results of this study can be found in the USGS final technical report (Treiman and others, 2010).[4]

Purpose

This study was intended to compare the utility of various imagery types in the identification of active surface faults. We have done comparative mapping of recently active surface traces of the San Andreas Fault in southern California using conventional aerial photography, digital elevation models (DEMs) from LiDAR (Light Detection and Ranging, also known as Airborne Laser Swath Mapping), recently acquired digital imagery (stereo and ortho-images), and satellite multi-spectral imagery.

[4]Research supported by the U.S. Geological Survey (USGS), Department of the Interior, under USGS award number 08HQGR0096.

Current methods of fault interpretation from aerial imagery, individually, have certain strengths and weaknesses. Vintage aerial photos provide stereo viewing and show the landform prior to extensive human modification but commonly lack color and have limitations in accuracy of location due to lack of georeferencing and the inherent distortions in the medium. LiDAR terrain data have high spatial resolution and accuracy that can reveal subtle geomorphic features, can be viewed as detailed shaded-relief images illuminated from any direction, and have the capability of removing vegetation (in a virtual sense). But this type of imagery is limited to the modern landscape, does not easily differentiate vegetation and cultural features from geologic features, and is relatively costly to acquire for new (not previously flown) areas. High resolution digital stereo imagery often can differentiate lithology, soil moisture content, and vegetation that can be useful for mapping the surface trace of active faults; however, as with traditional aerial photos, the ground surface can be obscured by vegetation. Multi-spectral imagery from several sources at varying resolutions makes advantageous use of single and multiple wavelengths of the electromagnetic spectrum but is also limited to the current landscape and requires considerable processing.

The value of LiDAR in areas with a tall, obscuring vegetation canopy has already been well demonstrated (Prentice and others, 2004; Whitehill and others, 2009). This study evaluates the relative value of LiDAR data in somewhat less densely vegetated terrain relative to several other types of imagery (photographic and digital). One objective of this study is to use the geographic precision of the digital imagery, especially LiDAR, to more accurately locate fault traces interpreted from vintage aerial photography and other imagery (typically plotted on 7.5-minute topographic base maps). A second objective is to merge the high-resolution LiDAR shaded relief with multi-spectral imagery, adding detailed topographic information to the unique surface information contained in spectral reflectance. By using several different types of imagery, we will judge which are more suitable for various field conditions.

Setting and Methodology

Two test areas of contrasting terrain and vegetation conditions were selected for this study. These two areas, shown on figure 1, are along the San Andreas Fault near the cities of Indio and Yucaipa, in southern California. The Indio area has very little vegetation, and so the surface morphology and character are visible in most imagery types. Strands of the fault lie partly along the abrupt southwest front of the Indio Hills and project southward beyond the hill front into more subdued desert terrain. Some of this area has been significantly modified by human activity. Secondary fault strands lie within the uplifted terrain of the Indio Hills. Geologic variation within the area is limited, with the main contrast

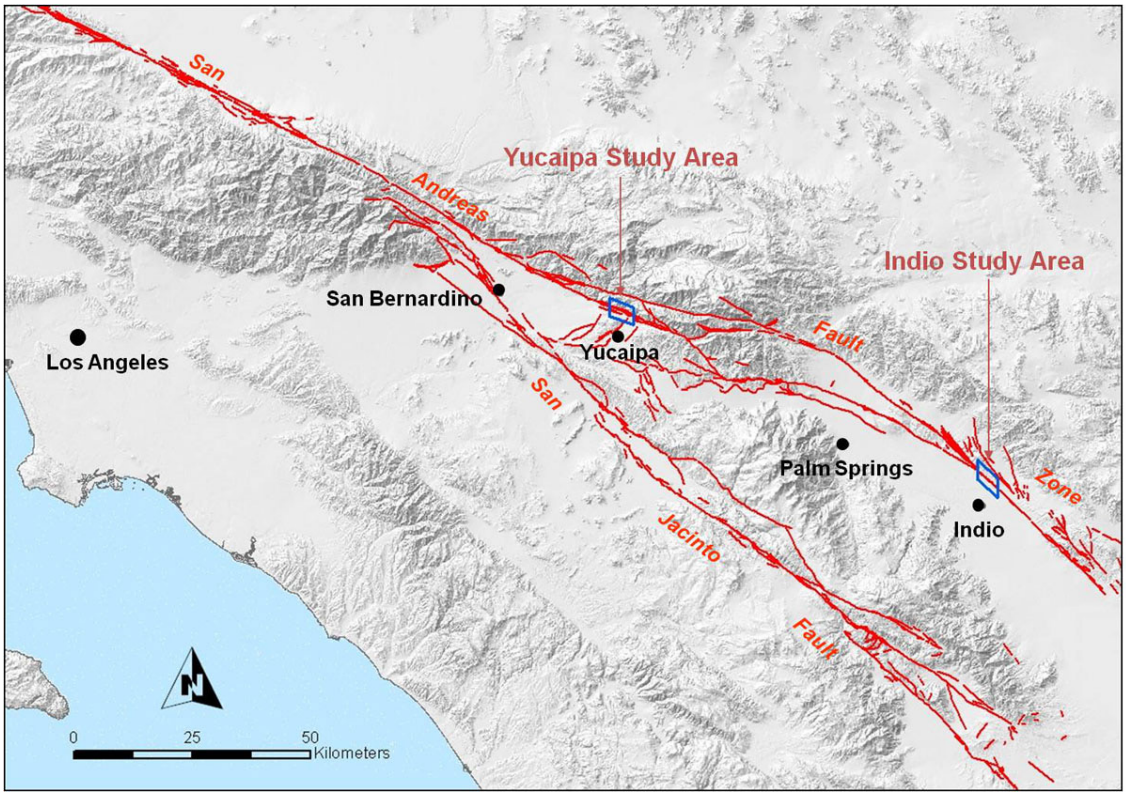

Figure 1. Index map of San Andreas Fault and the two study areas in southern California.

corresponding to the topographic front. The Yucaipa area differs from the Indio area in several aspects, most evident of which is the amount of vegetation growing on the slopes and associated thicker soil, which masks many of the finer fault features. Also, the faults in the Yucaipa area lie largely within uplifted terrain, with greater local relief than the Indio area. The underlying earth materials vary considerably, from bedrock to landslide to alluvium.

Several types of imagery were acquired and interpreted. These included standard black and white aerial photography, modern digital color imagery, and LiDAR-derived DEMs. Stereo viewing of the study areas was possible with standard aerial photography as well as with ADS40 (Aerial Digital Sensor) Stereo imagery. A three-dimensional (3D) view was effected with the LiDAR DEM (shaded relief) imagery. Each image type, alone and in selected combinations, was independently interpreted by a geologist for lineaments and other geomorphic features that could be associated with faulting. Interpretation was performed at a variety of scales to detect both large- and small-scale features.

The features interpreted from these types of imagery were compiled on separate map layers. A composite map was then prepared in order to consolidate into a best-fit location those features that were evidently the same. Faults interpreted from vintage aerial photos were not included in the composite map but were used to evaluate the completeness and accuracy of the composite fault map and served as a guide for subsequent field reconnaissance. Many "features" were plotted that did not correspond to any known faults. Features that were consistently observed across the various imagery types suggested the location of previously unmapped faults, or corroborated and helped to relocate other faults.

Limited field reconnaissance and mapping helped to further refine the baseline fault map, confirming or refuting some interpreted faults. In some field locations, additional geomorphic evidence of faulting was recorded that had not been observed in any of the imagery.

Two baselines of data are needed to compare the utility of the various imagery types. First is a baseline of the faults as previously mapped and presented in the published literature (figs. 2A and 2B). Improvements in fault mapping are judged against this base. Second is a map of revised fault locations. These maps were derived from the previous mapping, as revised to correspond with the more definitive evidence from this study (including both image interpretation and field reconnaissance). This second baseline fault map is used to judge the efficacy of each of the individual imagery types.

Assuming that the final revised fault locations are the best approximation of the actual fault pattern, we then measured how many linear meters of the fault traces had been identified using each imagery type. Conclusions were drawn from comparison of the relative utility of each imagery type for interpreting faults in a variety of terrain and vegetation conditions.

Remote Sensing Imagery

Six different types of imagery were acquired for this study: standard black and white aerial photographs, LiDAR digital elevation models, ADS40/NAIP color ortho-image, ADS40/ISTAR color-infrared ortho-image, ADS40 Stereo imagery, and ASTER imagery. These imagery types as well as their properties and characteristics are summarized in table 1.

In order to undertake a comparative analysis of the suitability of the different imagery for fault trace mapping, it is imperative that they are in a format that can be displayed, overlaid, analyzed, and digitized in a Geographic Information System (GIS) environment. It is essential therefore that the various imagery have the same areal extent or have some overlap, are georeferenced and co-registered, and have compatible file formats. Since the imagery acquired for this study was in a variety of file formats, pixel sizes, areal coverages, and coordinate systems, considerable preparation and processing had to be undertaken. Additionally, derivative imagery was extracted from the acquired imagery, and combination imagery was also generated by data fusion. Data fusion requires resampling, contrast stretching, and reprojection (Carter, 1998).

The processed and derived imagery used in the actual fault interpretation and evaluation is summarized in table 2.

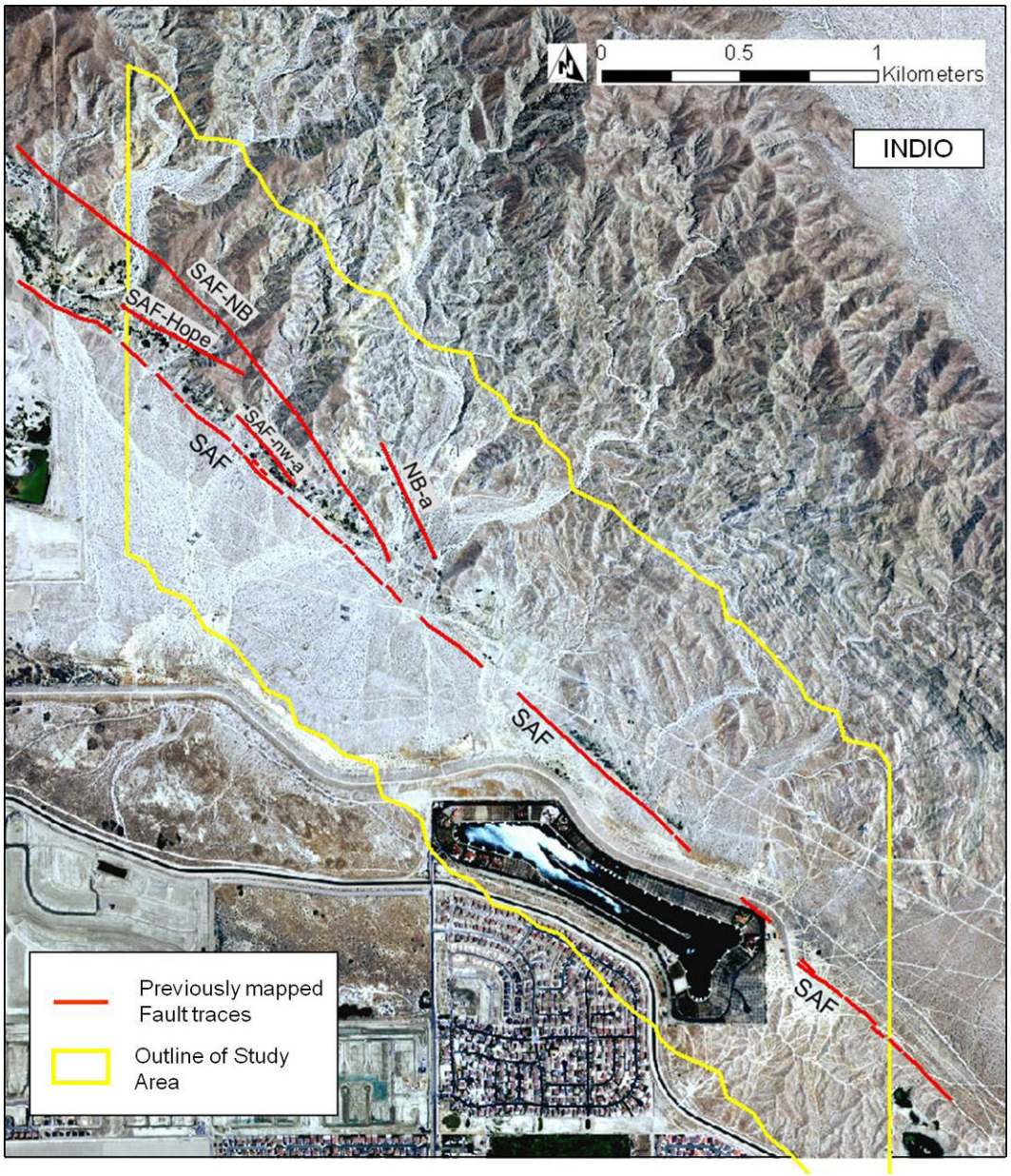

Figure 2A. Indio study area showing previously mapped fault traces. “SAF” refers to the San Andreas Fault; see Treiman and others (2010) for explanation of other identified fault traces.

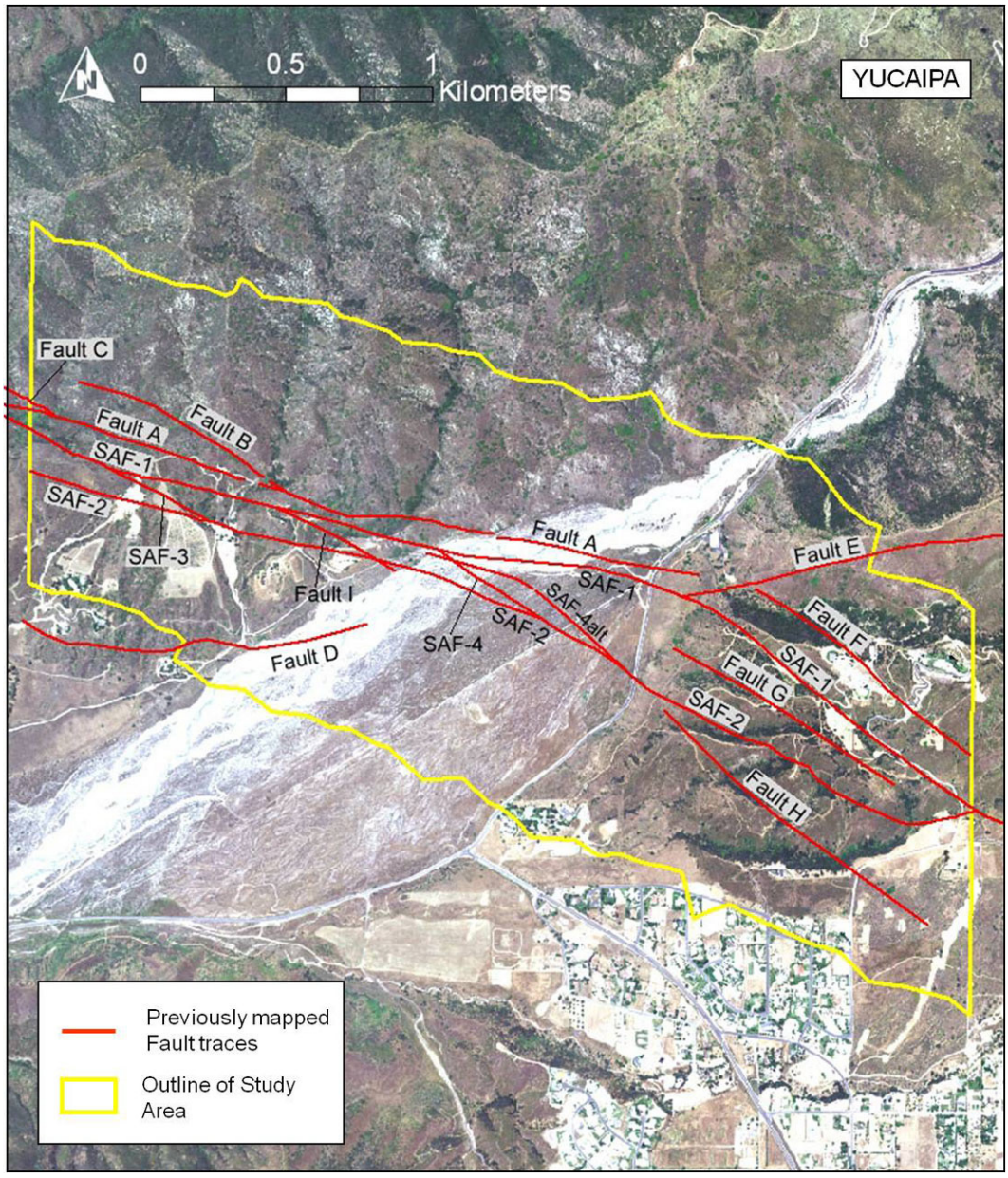

Figure 2B. Yucaipa study area showing previously mapped fault traces. "SAF" refers to the San Andreas Fault; see Treiman and others (2010) for explanation of other identified fault traces.

Table 1. Summary of properties and characteristics of the acquired imagery.

[RGB, red-green-blue; pan, panchromatic; NIR, near infrared; VNIR, very near infrared; SWIR, short wave infrared; TIR, thermal infrared; m, meter; cm, centimeter]

	IMAGERY (Acquisition Date)	Format/ Coverage	Scale/pixel resolution	Stereo	Rectified	Geolocated	Estimated/Stated Horiz. Accuracy	Spectral Bands	Unique Characteristics	File Format	Projection/ Datum
1	**Aerial Photos** (1930, 1953/54)	B&W Film/Paper 9 inch	~ 1:18000 ~1:20000	yes	no	no	same as warped imagery	1	pre-development photos, familiar character, sub-meter resolution in stereo.	paper JPEG TIFF	UTM, z11N NAD-83
2	**LiDAR DEM** (2005)	Digital Swath = 0.8 mi Variable length	0.5 m	no	yes	yes	10-20 cms	1	very high resolution topo with foliage penetration, 3D view, variable source of illumination.	ADF	UTM, z11N WGS-84
3	**ADS40/NAIP** (2005)	Digital Quarter Quads ~16 mi^2	1.0 m	no	yes	yes	5-10 m	3 (R,G,B)	synoptic coverage, natural color, vegetation and cultural features.	ADF, TIFF	UTM, z11 NAD-83
4	**ADS40/ISTAR** (2003)	Digital ~3 mi^2 tiles	0.5 m	no	yes	yes	1.5 m	3 Pan 4 RGB/NIR	visible and near infrared, vegetation type, soil saturation.	FLT, ADF, TIFF	UTM, z11N NAD-83
5	**ADS40 Stereo** (2005)	Digital 5 mi x 100 mi (stereo subsets can be extracted using Leica GPro)	1.0 m	yes	partial	yes	6.0 m	5 (Pan,R.G.B, NIR)	rapid imagery interpretation with feature collection and attribution in stereo, variable vertical exaggeration.	TIFF	LSR Anchored WGS-84
6	**ASTER** (2006)	Digital ~38 mi^2/scene	15 m 30 m 90 m	yes no no	no no no	yes yes yes	~25 m	3 VNIR 6 SWIR 5 TIR	spectral information can be transformed into other forms or space.	HDF, TIFF	UTM, z11N WGS-84

Table 2. Summary of the various image processing techniques used to generate the processed and derived imagery.

[TCC, True Color Composite; FCC, False Color Composite; VNIR, very near infrared]

ACQUIRED UNPROCESSED IMAGERY	IMAGERY PROCESSING / TRANSFORMATION ------ ------▶														DERIVED / PROCESSED IMAGERY		
																Combination	
	Scan	Mosaic	Warp	Georeference	Subset	Resample	Re-Project	Enhance	Contrast Stretch	Band Order	Topo Modeling	Layer Stacking	Data Fusion	Slice - GPro	Single	Draped over LiDAR DEM Shaded Relief	Fused with LiDAR DEM
Aerial Photos	x	x	x	x	x		x	x							Digital Aerial Photos		
LiDAR DEM		x			x			x			x				LiDAR DEM Shaded Relief		
ADS40/NAIP					x	x	x	x	x		x	x	x		ADS40/NAIP TCC	ADS40/NAIP TCC	ADS40/NAIP TCC
					x	x	x	x	x	x	x	x	x		ADS40/NAIP FCC	ADS40/NAIP FCC	ADS40/NAIP FCC
ADS40/ISTAR					x		x	x	x		x	x	x		ADS40/ISTAR TCC	ADS40/ISTAR TCC	ADS40/ISTAR TCC
					x		x	x	x	x	x	x	x		ADS40/ISTAR FCC	ADS40/ISTAR FCC	ADS40/ISTAR FCC
ADS40Stereo								x						x	ADS40 Stereo		
ASTER					x	x		x	x	x	x	x	x		ASTER VNIR	ASTER VNIR	ASTER VNIR

Results

Figures 3A and 3B present a consolidated plot of all of the geomorphic features interpreted for each study area. These features were used, along with previous mapping and field reconnaissance, to refine the previous fault trace locations and, in some instances, infer newly mapped traces. Many of the features were observed in more than one image, in which case a judgment was made as to the best representation for the consolidated plot.

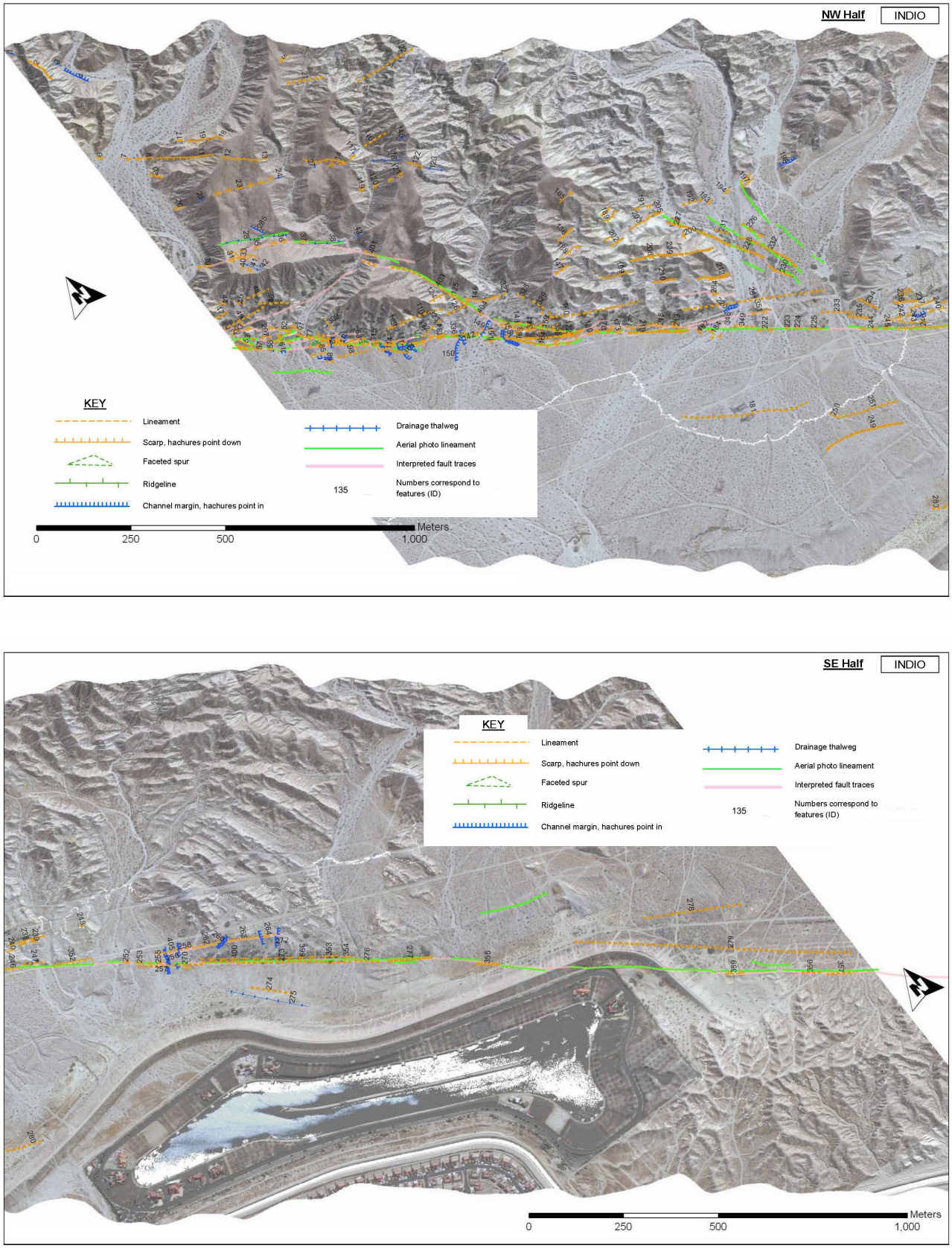

Figure 3A. Consolidated plot of fault-related geomorphic features interpreted in the Indio study area (upper figure is northwest half, lower figure is southeast half).

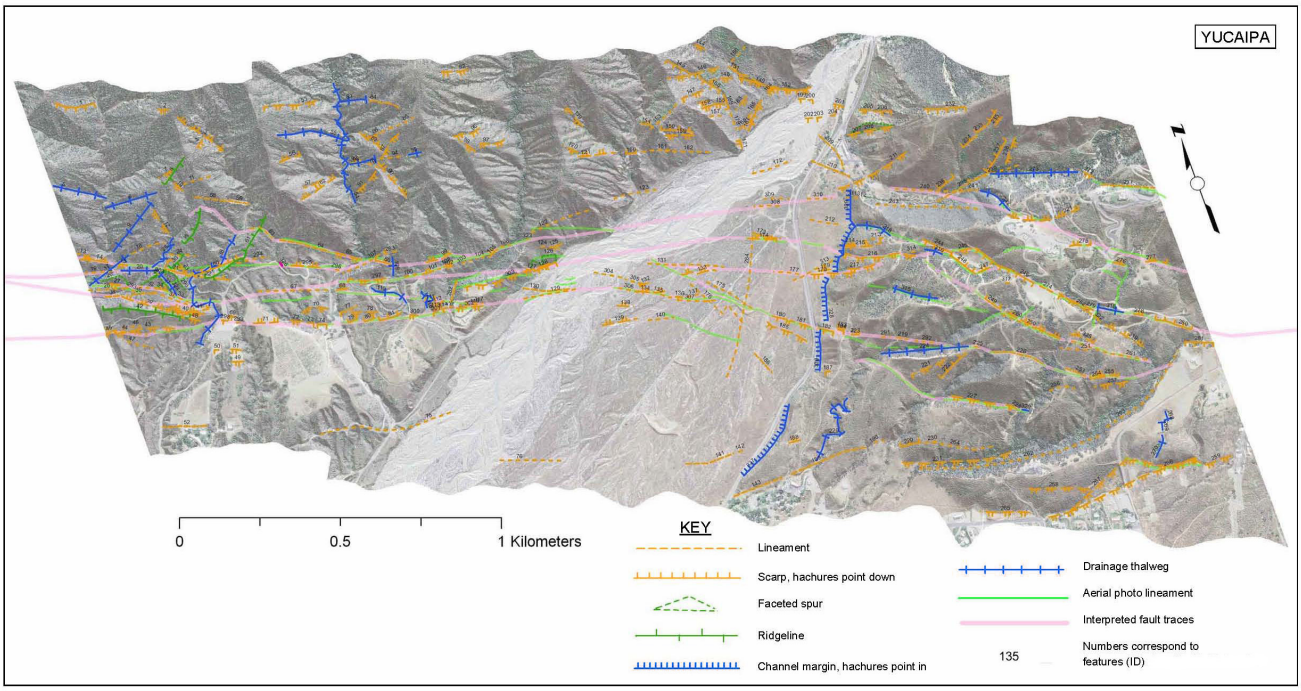

Figure 3B. Consolidated plot of fault-related geomorphic features interpreted in the Yucaipa study area.

Figures 4A and 4B show the reinterpreted faults used in this study, for the comparison of the different imagery types. Tables 3A and 3B-D show the raw numbers indicating the percent of the presumed fault trace lengths interpreted using each imagery type, for each of the two study areas. The totals for each area show that black and white stereo aerial photographs were most effective for mapping faults in either area, identifying 54 percent (Indio) to 50 percent (Yucaipa) of the accepted faults. In the sparsely vegetated Indio area, ADS40 Stereo imagery was nearly as effective (53 percent) whereas in the chaparral-covered Yucaipa area LiDAR was the next most effective imagery (40 percent). However, these are gross comparisons and more can be learned by focusing on sections of faulting that share common characteristics. The discussion below is confined to the most useful imagery. The results from the other imagery are compiled in the tables.

While the numbers in the tables provide some simplistic comparisons, they do not highlight whether the different imagery types were revealing more or less of the same traces or whether each had their own strengths, detecting fault segments not seen in other imagery. A more careful assessment of the results, considering area characteristics (geology, topography, and vegetation) and looking at each mapped fault trace revealed some trends but no overwhelmingly stark contrasts. Imagery types are ranked (based on percent of fault detected) for each fault segment, in tables 4A-D. For most areas, true stereo imagery (photographic or digital) detected the most fault traces. The character of the underlying geology does not appear to have a systematic impact that was detectable in this limited study.

Figure 4A. Interpreted fault traces in the Indio area.

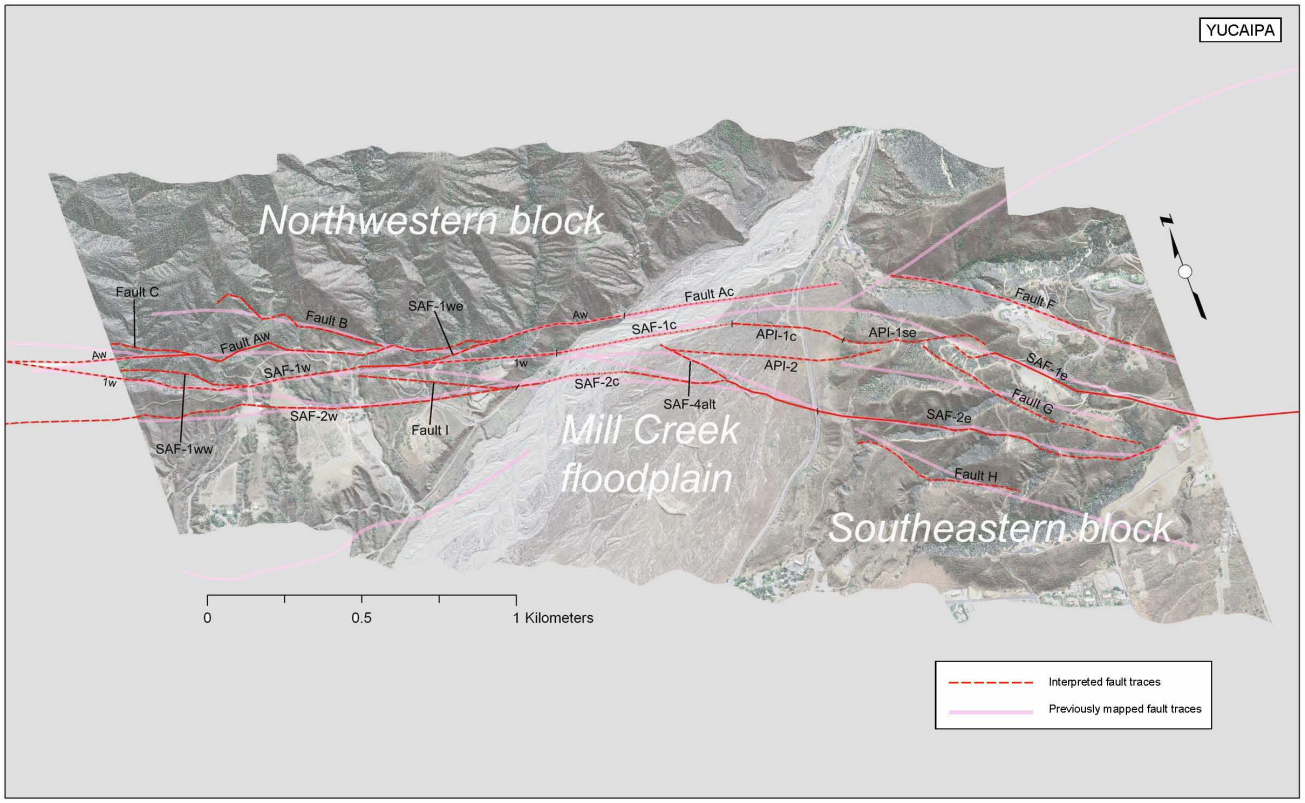

Figure 4B. Interpreted fault traces in the Yucaipa area.

Table 3A. Interpreted faults in the Indio study area showing the proportion of fault traces identified in each imagery type.

[Qal, younger alluvium and fan deposits; Qo, Ocotillo conglomerate; Qp, Palm Spring Formation; "/", indicates one unit faulted against the other; T, True Color Composite; F, False Color Composite]

Indio study area

INTERPRETED FAULTS			PROPORTION (Length and Percentage) OF FAULT TRACES IDENTIFIED IN EACH IMAGERY TYPE															
Fault Trace	Geology	Length meter (m)	Aerial Photo		LiDAR DEM		ADS40/NAIP		ADS40 Stereo		ASTER		Draped on LiDAR		Fused with LiDAR DEM			
													ADS40/NAIP		ADS40/NAIP T		ADS40/NAIP F	
			m	%	m	%	m	%	m	%	m	%	m	%	m	%	m	%
SAF-nw	Qp/Qal	2425	970	40%	820	34%	860	35%	1260	52%	915	38%	480	20%	575	24%	620	26%
SAF-c	Qp/Qal	1735	1155	67%	925	53%	905	52%	1180	68%	1050	61%	960	55%	615	35%	795	46%
SAF-se	Qal	1245	1050	84%	105	8%	180	14%	365	29%	845	68%	180	14%	165	13%	185	15%
SAF-NB(r)	Qo, Qp	555	210	38%	75	14%	0	0%	175	32%	0	0%	140	25%	205	37%	0	0%
SAF-nw-a	Qo, Qp	845	425	50%	285	34%	190	22%	660	78%	150	18%	185	22%	135	16%	85	10%
SAF-Hope(r)	Qp	330	0	0%	0	0%	90	27%	15	5%	0	0%	0	0%	0	0%	0	0%
NB-a	Qal	345	225	65%	0	0%	300	87%	325	94%	295	86%	335	97%	225	65%	235	68%
Sum	%	7480	4035	54%	2210	30%	2525	34%	3980	53%	3255	44%	2280	30%	1920	26%	1920	26%

Table 3B. Interpreted faults in the Yucaipa study area showing the proportion of fault traces identified in each imagery type.

[Qyf, younger alluvial fan deposits; Qof, older alluvial fan deposits; gg, gneissic basement rock; "/", indicates one unit faulted against the other; T, True Color Composite; F, False Color Composite]

Yucaipa, Northwest area – bedrock terrain

INTERPRETED FAULTS			PROPORTION OF FAULT TRACES (Length and Percentage) IDENTIFIED IN EACH IMAGERY TYPE																			
Fault Trace	Geology	Length meter (m)	Aerial Photo		LiDAR DEM		ADS40/NAIP		ADS40/ISTAR		ADS40 Stereo		Draped on LiDAR				Fused with LiDAR DEM					
													ADS40/NAIP		ADS40/ISTAR		ADS40/NAIP T		ADS40/NAIP F		ADS40/ISTAR	
			m	%	m	%	m	%	m	%	m	%	m	%	m	%	m	%	m	%	m	%
SAF-1w	gg/Qof, Qyf	1410	275	20%	650	46%	125	9%	0	0%	115	8%	345	24%	325	23%	90	6%	50	4%		
SAF-1ww	gg	415	330	80%	180	43%	0	0%	0	0%	240	58%	245	59%	0	0%	0	0%	190	46%		
SAF-1we	gg	275	280	102%	205	75%	125	45%	0	0%	215	78%	160	58%	0	0%	0	0%	35	13%		
SAF-2w	Qof, Qyf	1250	610	49%	450	36%	0	0%	0	0%	455	36%	375	30%	450	36%	540	43%	440	35%		
Fault Aw	gg, Qyf	1685	1200	71%	815	48%	470	28%	0	0%	840	50%	520	31%	105	6%	160	9%	215	13%		
Fault B	gg	600	240	40%	390	65%	150	25%	135	23%	330	55%	370	62%	180	30%	0	0%	0	0%		
Fault C	gg	270	145	54%	150	56%	0	0%	0	0%	0	0%	0	0%	0	0%	120	44%	0	0%		
Fault I	Qof, Qyf	455	340	75%	150	33%	0	0%	0	0%	0	0%	35	8%	85	19%	0	0%	25	5%		
Sum	%	6360	3420	54%	2990	47%	870	14%	135	2%	2195	35%	2050	32%	1145	18%	910	14%	955	15%	0	0%

Table 3C. Interpreted faults in the Yucaipa study area showing the proportion of fault traces identified in each imagery type.

[Qal, young and modern stream channel deposits of Mill Creek; Qoal, older flood plain and channel deposits of Mill Creek]

Yucaipa, Central area – alluvial flood plain of Mill Creek

INTERPRETED FAULTS			PROPORTION OF FAULT TRACES (Length and Percentage) IDENTIFIED IN EACH IMAGERY TYPE																			
Fault Trace	Geology	Length meter (m)	Aerial Photo		LiDAR DEM		ADS40/NAIP		ADS40/ISTAR		ADS40 Stereo		Draped on LiDAR				Fused with LiDAR DEM					
													ADS40/NAIP		ADS40/ISTAR		ADS40/NAIP T		ADS40/NAIP F		ADS40/ISTAR	
			m	%	m	%	m	%	m	%	m	%	m	%	m	%	m	%	m	%	m	%
SAF-1c	Qal	585	0	0%	380	65%	0	0%	0	0%	30	5%	50	9%	0	0%	0	0%	0	0%		
API-1c	Qoal	370	175	47%	0	0%	0	0%	0	0%	0	0%	140	38%	0	0%	0	0%	0	0%		
SAF-2c	Qal, Qoal	1000	730	73%	200	20%	90	9%	135	14%	410	41%	175	18%	80	8%	100	10%	100	10%	170	17%
Fault Ac	Qal, Qoal	710	0	0%	0	0%	0	0%	0		175	25%	0		0	0%	0	0%	0	0%		
Fault-API-2	Qoal	690	0	0%	220	32%	190	28%	255	37%	0	0%	325	47%	0	0%	275	40%	250	36%		
SAF-4alt	Qoal	240	190	79%	0	0%	65	27%	0	0%	0	0%	0	0%	0	0%	0	0%	0	0%		
Sum	%	3595	1095	30%	800	22%	345	10%	390	11%	615	17%	690	19%	80	2%	375	10%	350	10%	170	5%

Table 3D. Interpreted faults in the Yucaipa study area showing the proportion of fault traces identified in each imagery type.

[landslide deposits derived from Mill Creek Formation]

Yucaipa, Southeast area – landslide disturbed bedrock terrain

INTERPRETED FAULTS			PROPORTION OF FAULT TRACES (Length and Percentage) IDENTIFIED IN EACH IMAGERY TYPE																			
Fault Trace	Geology	Length meter (m)	Aerial Photo		LiDAR DEM		ADS40/NAIP		ADS40/ISTAR		ADS40 Stereo		Draped on LiDAR				Fused with LiDAR DEM					
													ADS40/NAIP		ADS40/ISTAR		ADS40/NAIP T		ADS40/NAIP F		ADS40/ISTAR	
			m	%	m	%	m	%	m	%	m	%	m	%	m	%	m	%	m	%	m	%
SAF-1e	landslide	840	725	86%	590	70%	170	20%	0	0%	565	67%	280	33%	0	0%	240	29%	370	44%		
API-1se	landslide	470	250	53%	420	89%	0	0%	0	0%	245	52%	115	24%	0	0%	260	55%	140	30%		
SAF-2e	landslide	1140	525	46%	535	47%	280	25%	40	4%	385	34%	410	36%	0	0%	405	36%	500	44%		
Fault F	landslide	960	340	35%	0	0%	0	0%	0	0%	125	13%	70	7%	0	0%	0	0%	175	18%		
Fault G	landslide	780	555	71%	350	45%	255	33%	0	0%	460	59%	190	24%	185	24%	445	57%	320	41%		
Fault H	landslide	570	510	89%	210	37%	195	34%	0	0%	210	37%	165	29%	205	36%	255	45%	275	48%		
Sum	%	4760	2905	61%	2105	44%	900	19%	40	1%	1990	42%	1230	26%	390	8%	1605	34%	1780	37%	0	0%

Table 4A. Imagery types with rankings of effectiveness for mapping each fault trace. Effectiveness is based on the percentage of lineal fault length identified in each imagery type.

[Qal, younger alluvium and fan deposits; Qo, Ocotillo conglomerate; Qp, Palm Spring Formation; "/", indicates one unit faulted against the other; T, True Color Composite; F, False Color Composite]

Indio study area

Fault Trace	TERRAIN / FIELD Conditions				Imagery Type							Best Imagery
	Slope	Vegetation	Geology	Remarks	AP	LiDAR	NAIP	STEREO	Draped NAIP	Fused NAIP T	Fused NAIP F	
SAF-nw	low to moderate	light to moderate	Qp/Qal	multiple traces that are close together	4	4	4	3	5	5	5	STEREO with AP, LiDAR, NAIP
SAF-c	low to moderate	light	Qp/Qal		2	3	3	2	3	4	4	AP or STEREO
SAF-se	low	light	Qal	modified landscape	1		5	4	5	5	5	AP
SAF-NB(r)	low to mod to steep	light	Qo, Qp		4	5		4	5	4		AP, f-NAIP with STEREO
SAF-nw-a	low to moderate	low to moderate	Qo, Qp	parallel traces, oases	3	4	5	1	5	5	5	STEREO
SAF-Hope(r)	low to moderate	light to moderate	Qp	truncated old fans, oases			4					Field
NB-a	low	sparse	Qal, Qp	contrasting lithology	2		1	1	1	2	2	Color Imagery (NAIP,d-NAIP or STEREO)

Range	1	2	3	4	5
Percent range	75-100	60-74	50-59	26-49	10-25

Table 4B. Imagery types with rankings of effectiveness for mapping each fault trace. Effectiveness is based on the percentage of lineal fault length identified in each imagery type.

[Qyf, younger alluvial fan deposits; Qof, older alluvial fan deposits; gg, gneissic basement rock; "/", indicates one unit faulted against the other; T, True Color Composite; F, False Color Composite]

Yucaipa study area – northwest block

Fault Trace	TERRAIN / FIELD Conditions				Imagery Type									Best Imagery
	Slope	Vegetation	Geology	Remarks	AP	LiDAR	NAIP	ISTAR	STEREO	Draped NAIP	Draped ISTAR	Fused NAIP T	Fused NAIP F	
SAF-1w	moderate to high	moderate to dense	gg/Qof, Qyf	separates geologic units	5	4				5	5			LiDAR
SAF-1ww	moderate	moderate	gg/Qof, Qyf	faceted slopes	1	4			3	3			4	AP
SAF-1we	moderate	light to moderate	gg	alignment of features	1	1	4		1	3			5	AP or Stereo, LiDAR
SAF-2w	moderate to low	light to moderate	Qof, Qyf		4	4			4	4	4	4	4	all together
Fault-Aw	moderate to high	moderate	gg, Qyf	offset streams, ridges	2	3	4		3	4			5	AP with STEREO, LiDAR
Fault B	high to moderate	light to moderate	gg		4	2	4	5	3	2	4			LiDAR
Fault C	moderate to high	light to mod to dense	gg	hillslope features	3	3						4		AP or LiDAR
Fault I	moderate	light to medium dense	Qof, Qyf	manmade structures	1	4					5		5	AP

Range	1	2	3	4	5
Percent range	75-100	60-74	50-59	26-49	10-25

Table 4C. Imagery types with rankings of effectiveness for mapping each fault trace. Effectiveness is based on the percentage of lineal fault length identified in each imagery type.

[Qal, young and modern stream channel deposits of Mill Creek; Qoal, older flood plain and channel deposits of Mill Creek; T, True Color Composite; F, False Color Composite]

Yucaipa study area – central block

Fault Trace	TERRAIN / FIELD Conditions				Imagery Type									Best Imagery
	Slope	Vegetation	Geology	Remarks	AP	LiDAR	NAIP	ISTAR	STEREO	Draped		Fused		
										NAIP	ISTAR	NAIP T	NAIP F	
SAF-1c	low	light	Qal	modern, active channels		2								LiDAR
API-1c	low	moderate	Qoal	older inactive channels	4	4				4				AP, LiDAR, d-NAIP
SAF-2c	low	moderate	Qal, Qoal	modern, active channels	2	5		5	4	5		5	5	AP
Fault-Ac	low	light	Qal, Qoal	modern, active channels					5					Stereo
Fault-API-3	low	moderate	Qoal	older, inactive channels		4	4	4		4		4	4	NAIP or ISTAR and d-NAIP or f-NAIP
SAF-4alt	low	moderate	Qoal	older, inactive channels	1		4							AP

Range	1	2	3	4	5
Percent range	75-100	60-74	50-59	26-49	10-25

Table 4D. Imagery types with rankings of effectiveness for mapping each fault trace. Effectiveness is based on the percentage of lineal fault length identified in each imagery type.

[landslide deposits derived from Mill Creek Formation; Qoal, older flood plain and channel deposits of Mill Creek; T, True Color Composite; F, False Color Composite]

Yucaipa study area – southeast block

Fault Trace	TERRAIN / FIELD Conditions				Imagery Type									Best Imagery
	Slope	Vegetation	Geology	Remarks	AP	LiDAR	NAIP	ISTAR	STEREO	Draped		Fused		
										NAIP	ISTAR	NAIP T	NAIP F	
SAF-1e	moderate to high	moderate to dense	landslide	sag pond	1	2	5		2	4		4	4	AP STEREO/ LiDAR
API-1se	moderate to high	moderate to dense	landslide		3	1			3	5		3	4	LiDAR
SAF-2e	high to moderate	moderate to dense	landslide		4	4	4		4	4		4	4	LiDAR, AP or f-NAIP
Fault-F	moderate to high	moderate to dense	landslide		4				5				5	AP
Fault-G	moderate	moderate to dense	Qoal		2	4	4		3	5	5	3	4	AP
SAF-H	moderate	moderate to dense	landslide	sidehill bench	1	4	4		4	4	4	4	4	AP

Range	1	2	3	4	5
Percent range	75-100	60-74	50-59	26-49	10-25

Conclusions

Although there are no overwhelming trends, this study demonstrated that true stereo (ADS40 Stereo and vintage stereo photographs) was often the best imagery for identifying faults in terrain with topographic relief, whereas the LiDAR DEM offered advantages in terrain with moderate to heavy vegetation. If the clear advantage that vintage aerial photography has in areas that were subsequently modified is removed, ADS40 Stereo seemed to be the superior imagery for observing faults in areas of light vegetation. This advantage over vintage aerial photography is probably a result of the higher resolution of the digital imagery, with some additional benefit due to variable vertical exaggeration and adjustable brightness and contrast. In areas of heavier vegetation, LiDAR and vintage aerial photography were the more useful imagery.

There were always exceptions, and most other imagery or combinations certainly added fault elements not seen in the three principal platforms. However, these exceptions were often not clearly attributable to conditions of vegetation, relief, or geology, although the ability to see vegetation lineaments (using ISTAR and NAIP) proved advantageous in otherwise low-relief areas. Digital imagery (LiDAR or ADS40) with high resolution (1 m pixel or less) provides the best accuracy for fault location and is very useful for improving fault locations identified from either published mapping or aerial photo interpretation. Image types other than LiDAR had an advantage of sensing tonal differences, which often helps to define, connect, extend, or reinforce geomorphic lineaments. The low resolution of the ASTER data, even when fused with the LiDAR DEM shaded relief, seriously hampered its usefulness to a mapping effort at the scale made possible by the other imagery.

Ultimately, we believe that it was the use of multiple image types that allowed greater completeness of fault trace mapping in the areas studied, with an increase in accuracy of location dependent on the type of digital imagery available. Observation of a trace using several image types provided reinforcing evidence for fault interpretation. Even small fault elements, uniquely identified in one image type, when viewed in aggregate with other imagery, provided necessary continuity to lineament interpretation. Draped or fused imagery added value for some faults, but the additional processing involved in the fusion process may not be justified by the minimal improvements seen in this study. The identification of some strong lineaments that probably are not fault related also reinforced the need for ground truth in any geologic studies.

LiDAR data are freely available, but only along specific narrow swaths where data have already been collected (*http://www.opentopography.org*). This can be frustrating where unanticipated splay faults and local complications extend beyond the LiDAR coverage. ADS40 Stereo imagery currently exists for the entire State of California; wider availability is being considered. The results of this study show that investment in making these data more readily available and usable can have significant benefits for many mapping interests, including fault mapping.

Acknowledgments

We wish to acknowledge the assistance of our colleagues at the California Geological Survey: Tim McCrink for his invaluable assistance in working with the ADS40 stereo imagery in stereo analyst and in imagery slicing; Carlos Gutierrez for ArcGIS database management and troubleshooting; and Chuck Real, Tim McCrink, and Chris Wills for advice, support and critical review of the manuscript.

Sincere thanks are due to the Open Topography team led by Chris Crosby (San Diego Supercomputing Center, Geoscience Coordinator & OpenTopography lead, GEON Project) who provided assistance and guidance in the acquisition of LiDAR imagery.

We are indebted to Jonathan Matti, at the U.S. Geological Survey, who made the 1930 Spence aerial photos available for our use in the Yucaipa area. We also benefited from the knowledge he shared about the geology and structure of the area and the encouragement to pursue our own findings.

References

Carter, D.B., 1998, Analysis of multiresolution data fusion techniques: Unpublished M.S. thesis, Virginia Polytechnical Institute and State University, 54 p.

Popenoe, F.W., 1959, Geology of the southeastern portion of the Indio Hills, Riverside County, California: Unpublished M.A. thesis, UCLA, 153 p., map scale 1:31,250.

Prentice, C.S., Koehler, R.D. III, Baldwin, J.N., Harding, D.J., 2004, Evaluation of LiDAR imagery as a tool for mapping the northern San Andreas Fault in heavily forested areas of Mendocino and Sonoma Counties, California (abs.): EOS, Transactions of the American Geophysical Union, v. 85, no. 47, Fall Meeting Supplement, Abstract G11B-07.

Treiman, J.T., Perez, F.G., and Bryant, W.A., 2010, Utility of combined aerial photography and digital imagery for fault trace mapping in diverse terrain and vegetation regimes: Final Technical report to U.S. Geological Survey, National Earthquake Hazards Reduction Program, award number 08HQGR0096, 57 p., *http://earthquake.usgs.gov/research/external/reports/08HQGR0096.pdf*.

Whitehill, C.S., Prentice, C.S., and Mynatt, I., 2009, LiDAR-based mapping of the northern San Andreas and Hayward Faults, California (abs.): Seismological Research Letters, v. 80, no. 2, p. 304.